

Defects or not defects ? Or how to design 20 - 25 nm spherical iron oxide nanoparticles to harness both magnetic hyperthermia and photothermia

Barbara Freis^{1,2}, Céline Kiefer¹, Sébastien Harlepp^{3,4,5}, Maria De Los Angeles Ramirez¹, Damien Mertz¹, Cristian Iacovita^{6,*}, Sophie Laurent², Sylvie Bégin^{1,*}

1 – Université de Strasbourg, CNRS, Institut de Physique et Chimie des Matériaux, UMR CNRS-UdS 7504, 23 Rue du Loess, BP 43, 67034 Strasbourg, France

2 – Laboratoire de NMR et d'imagerie moléculaire, Université de Mons, Avenue Maistriau 19, 7000 Mons, Belgium

3- Institut de Cancérologie Strasbourg Europe, 67000 Strasbourg, France

4.Equipe Labellisée Ligue Contre le Cancer

5.Strasbourg Drug Discovery and Development Institute (IMS), 67000 Strasbourg, France

6- Department of Pharmaceutical Physics-Biophysics, Faculty of Pharmacy, Iuliu Hatieganu University of Medicine and Pharmacy, 6 Pasteur St., 400349 Cluj-Napoca, Romania

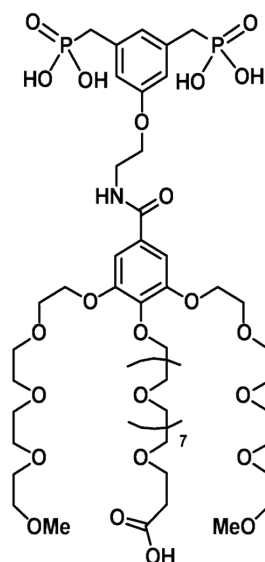


Figure S1: Dendron molecule D1-2P.

Table S1: Synthesis conditions and results obtained using the first protocol, denoted as P20_1, along with the use of homemade FeSt₃. T1 represents the temperature within the flask during the first step, where the reagent is dissolved, while T2 represents the final reaction temperature within the flask, which is the highest temperature maintained for a duration of 2h during the synthesis. The MALDI-TOF analysis has been conducted as described in reference ³¹ and allowed identifying the main polycations in home-made FeSt₃.

	NP_P20_1_A	NP_P20_1_B	NP_P20_1_C	NP_P20_1_D
FeSt ₃	FeSt ₃ -1	FeSt ₃ -2	FeSt ₃ -3	FeSt ₃ -4
T1 (°C)	125	124	122	122

T2 (°C)	331	342	331	326
Mean TEM size (nm)	19.1 ± 2.1	15.6 ± 1.5	26.9 ± 1.9	17.1 ± 1.6
XRD Crystallite size (nm)	17.7 ± 1	15.0 ± 1	/	14.5 ± 1
Lattice parameter (Å)	8.383 ± 0.001	8.385 ± 0.001	/	8.388 ± 0.001
Carboxylate coordination (IR)	Bridging	Bridging	Bridging & Chelating	Bridging & Chelating
MALDI TOF	Fe ₃ O, Fe ₄ O ₇ Fe ₅ O ₂ and Fe ₇ O ₇	Fe ₇ O ₇	Fe ₃ O, Fe ₄ O ₇ Fe ₅ O ₂ and Fe ₇ O ₇	Fe ₃ O, Fe ₄ O ₇ Fe ₅ O ₂ and Fe ₇ O ₇

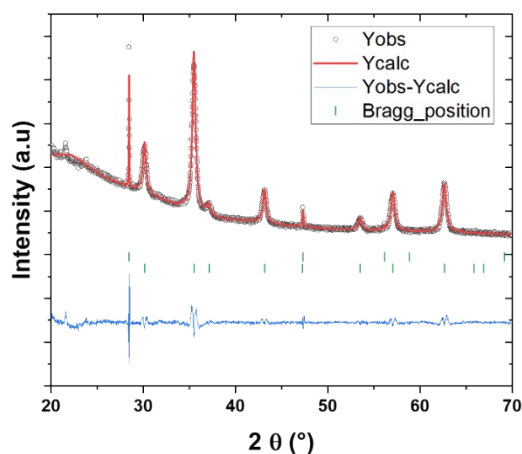


Figure S2: XRD pattern and refinement plot with Bragg positions for IONPs NP_P20_1_A synthesized using protocol P20_1 and FeSt3-1.

Analysis of the homemade precursors structure

IR spectra: The coordination of the carboxylate in the IR spectra of FeSt₃ has been compared, revealing dissimilarities among different FeSt₃ batches, as depicted in Figure S3A. Specifically, an examination of the IR bands within the range of 1800 cm⁻¹ and 1300 cm⁻¹ revealed noticeable variations in carboxylate coordination between batches (Figure S3B). For FeSt₃-1, FeSt₃-2, and FeSt₃-TCI, carboxylates primarily adopt a bridging coordination, whereas for FeSt₃-3 and FeSt₃-4, both chelating and bridging coordination are identified. Notably, the chelating carboxylate bands are slightly more pronounced in FeSt₃-3 and FeSt₃-4, suggesting a higher prevalence of chelating COOH coordination compared to earlier batches of iron stearates. These differences in coordination are likely to impact the decomposition of the iron stearate and, consequently, the size of resulting NPs. Furthermore, it is

worth noting another significant difference in the form of an IR band appearing around 1700 cm^{-1} corresponding to the C=O bond in an acid. This band is consistently present in homemade stearates, suggesting the existence of free stearic acid. In contrast, the commercial batch exhibits minimal or no presence of this band, indicating a lower quantity of free stearic acid. This disparity in free stearic acid content may also influence the thermal decomposition process and the ultimate size of the NPs produced during synthesis, as free stearic acid can potentially serve as a surfactant for the NPs¹.

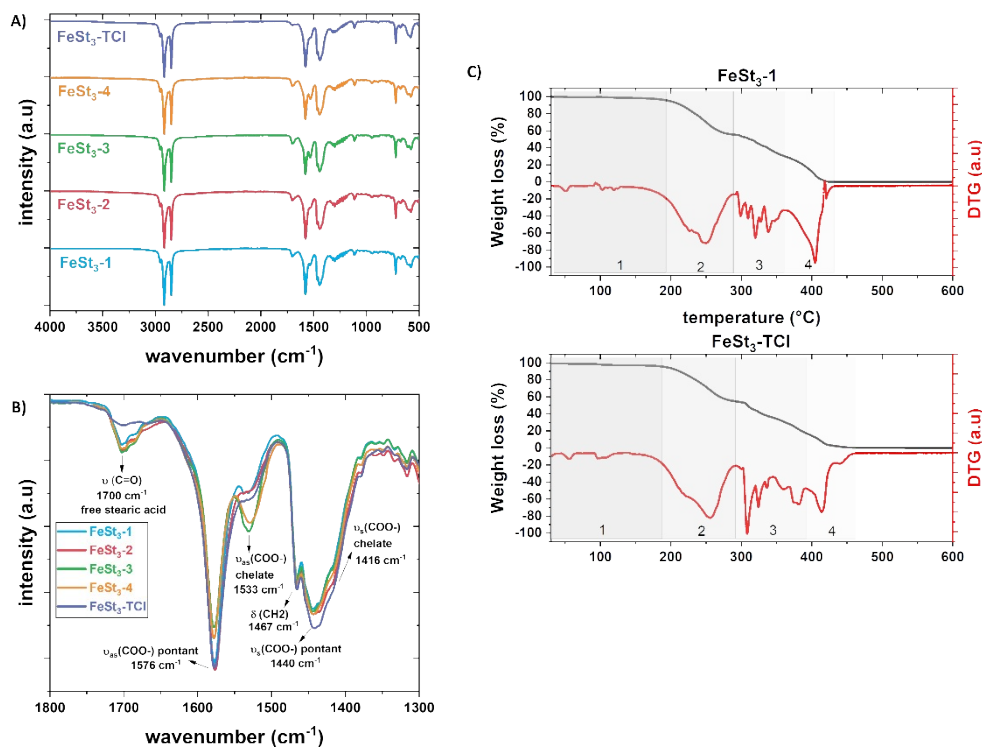


Figure S3: IR spectra of all batches of FeSt₃ A) from 4000 cm^{-1} to 400 cm^{-1} B) zoomed from 1800 cm^{-1} to 1300 cm^{-1} C) TGA/DTA curves of FeSt₃-1 and FeSt₃-TCl batches.

TGA/DTA analysis: TGA/DTA analyses were performed on the five batches of FeSt₃ aiming to analyze their decomposition as the temperature increase. TGA curves illustrated the percentage of the weight loss as the temperature rises, while DTA curves represent the first differentiation of the weight loss. Typically, TGA/DTA studies yield four distinct zones, as depicted in Figure S3C¹⁻⁶. The first zone, occurring below 150°C , and accounting for 2-3 weight loss, is attributed to the evaporation of water. The second zone, which constitutes around 50% of the weight loss, marks the nucleation stage and is attributed to the departure of stearate chains^{1-3,5,7}. This process is critical for germination during the TD synthesis and takes place in the temperature range 180°C - 280°C . The subsequent weight loss in the third zone is associated with the presence of larger polycations (containing a higher iron amount), which have different thermal stability and thus decompose at higher temperatures, ranging from 290°C to 360°C . This stage leads to the growth of the NPs through further decomposition of polycations, generating monomers. Finally, the fourth zone, which is the last phase of weight loss, corresponds to the degradation and burning of the organic chains, ultimately resulting in the production iron III oxide Fe₂O₃. The overall weight loss is similar among all the batches studied using TGA (whether they were homemade or commercial). However, variations, particularly in the temperature range of the third zone, were observed. In Figure S3C, for instance, the commercial batch

displayed a broader temperature range for this zone, indicating that, it decomposes over a wider temperature range and at higher temperatures. Consequently, more precursors were available for growth stage compared to FeSt₃-1. Similar trends were observed for FeSt₃-2 and other batches of homemade FeSt₃ not included in this study. It is important to note that this behavior was not consistent across all homemade FeSt₃ batches.

These characterizations of homemade batches clearly showed dissimilarities, as they exhibit variations in terms of carboxylate coordination, the type of polycations, and thermal stability. The homemade synthesis of FeSt₃ is particularly delicate in comparison to FeSt₂, mainly because of the larger iron polycations present in FeSt₃. Achieving consistent control over the polycations seems to be more intricate during the homemade synthesis of FeSt₃, which is why we opted to use the commercial batch for further experiments.

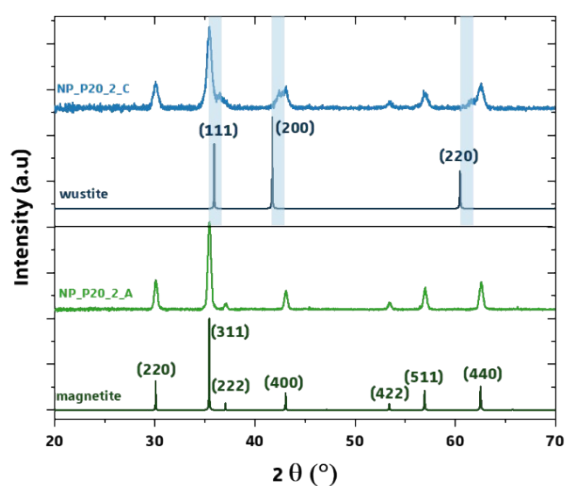
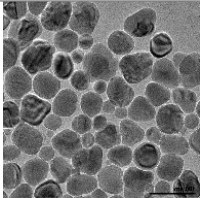
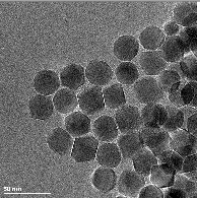
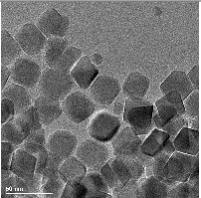
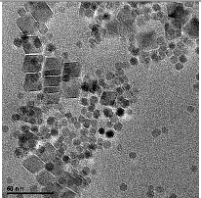
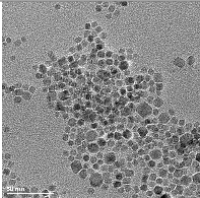
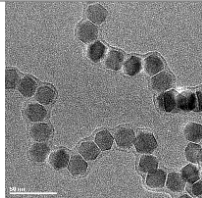


Figure S4. X-ray diffractograms of IONPs synthesized using the P20_2 protocol compared to theoretical diffractograms of the wüstite and the magnetite phases.

Table S2: Synthesis results obtained with the protocol P20_DBE and variation of DBE amount. T1 corresponds to the temperature in the flask during the first step to dissolve reagent and T2 correspond to the final reaction temperature.

Synthesis	NP_P20_DBE_no_DBE	NP_P20_DBE_0.5	NP_P20_DBE_1	NP_P20_DBE_2	NP_P20_DBE_5	NP_P20_DBE_10
						
FeSt₃	FeSt ₃ -TCl	FeSt ₃ -TCl	FeSt ₃ -TCl	FeSt ₃ -TCl	FeSt ₃ -TCl	FeSt ₃ -TCl
DBE (mL)	0	0.5	1	2	5	10
Squalane (mL)	20	19.5	19	18	15	10
T1 (°C)	120	127	127	111	119	118
T2 (°C)	327	338	339	328	305	271
Mean TEM size (nm)	50.6 ± 16.1	26.7 ± 1.6	32.1 ± 2.9	17.9 ± 0.9 and 7.6 ± 0.8	7.0 ± 1.1	21.6 ± 1.3
XRD crystallite size (nm)	/	26.5 ± 1	26.3 ± 1	/	6.7 ± 1	15.2 ± 1
Ratio crystallite size on TEM size	/	0.99	0.82	/	0.96	0.70
Cell parameter	/ Wüstite presence	8.393 ± 0.001	8.388 ± 0.001	8.389 ± 0.001	8.363 ± 0.001	8.382 ± 0.001

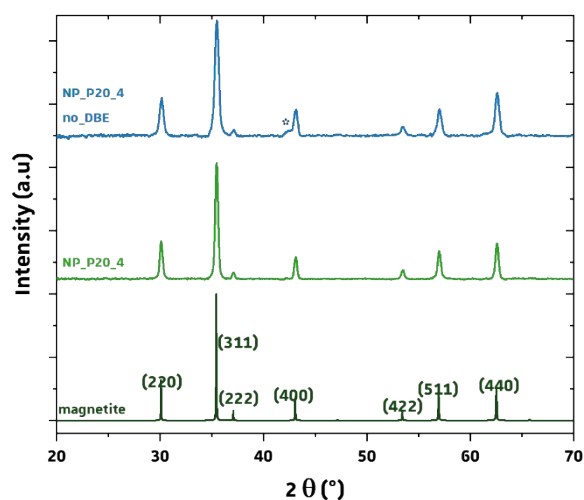


Figure S5: X-ray diffractograms of IONPs made using protocol P20_3 with and without DBE compared to theoretical peak of magnetite. A small peak which may contribute for a slight presence of wüstite is noted with a star for the synthesis NP_P20_3_no_DB.

Table S3. Repeatability studies using protocol P20_3_no_BDE.

Synthesis	NP_P20_3_no_DB_1	NP_P20_3_no_DB_2	NP_P20_3_no_DB_3	NP_P20_3_no_DB_4
FeSt ₃	FeSt ₃ -TCl	FeSt ₃ -TCl	FeSt ₃ -TCl	FeSt ₃ -TCl
T1 (°C)	121	117	119	115
T _{nucl} (°C)	282	275	277	277
T2 (°C)	326	320	322	321
Mean TEM size (nm)	25.4 ± 3.0	27.3 ± 3.0	22.9 ± 2.1	23.7 ± 3.0
XRD crystallite size (nm)	23.3	/	19.2 ± 1	17.8 ± 1
Lattice parameter (Å)	8.393	/(wüstite)	8.391 ± 0.001	8.385 ± 0.001
Ratio crystallite size on TEM size	0.92	/	0.84	0.75

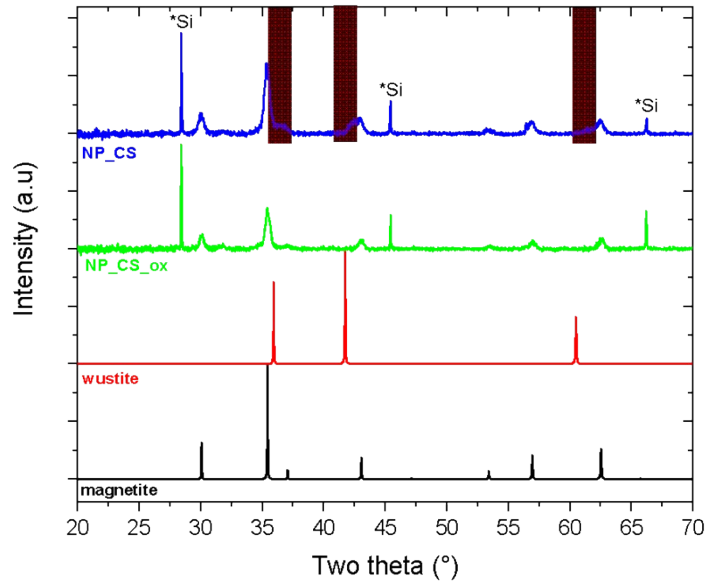


Figure S6. X-ray diffractograms of IONPs with a core shell composition ($Fe_{1-y}O@Fe_{3-x}O_4$) before and after oxidation treatment compared to theoretical peak of magnetite.

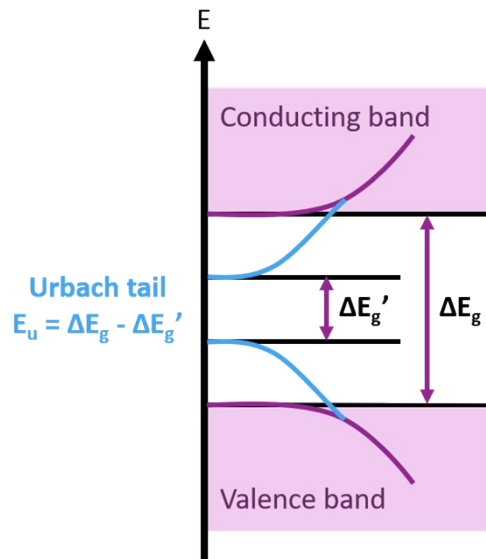


Figure S7: Schematic representation of the band gap and Urbach tail in presence of structural defects.

From the absorbance spectra obtained (Figure S9), E_g can be directly easily extracted from the Tauc equation:

$$(\alpha h\nu)^\gamma = A (h\nu - E_g)^\#(1)$$

where α is the absorption coefficient in cm^{-1} of the sample, h is the Planck constant equal to 6.63×10^{-34} J.s $^{-1}$, ν is the photon frequency and equals to the speed of light in vacuum divided by the photon wavelength λ and expressed in s $^{-1}$, A is a proportionality constant, E_g is the band gap energy in J or eV that we want to calculate and γ is a factor denoting the nature of electron transition which equals to 2 for band-gap semiconductors which have direct allowed transitions, which is our case here.

The absorption coefficient α can be determined from the Beer-Lambert law:

$$I = I_0 e^{-\alpha l} \quad \#(2)$$

I_0 is the incident light that encounters the sample, I is the transmitted light and l is the thickness of the cuve which is equal to 1 cm. Knowing that $\log \log \left(\frac{I_0}{I} \right)$ corresponds to the measured absorbance of the sample, the Beer-Lambert law can be rearranged, and the absorption coefficient is equal to $2,302 * A$.

From this equation, the Tauc plot $((\alpha h\nu)^2$ as a function of energy $h\nu$) can be plotted to determine E_g value by interpolating the linear part of the curve to the energy axis.

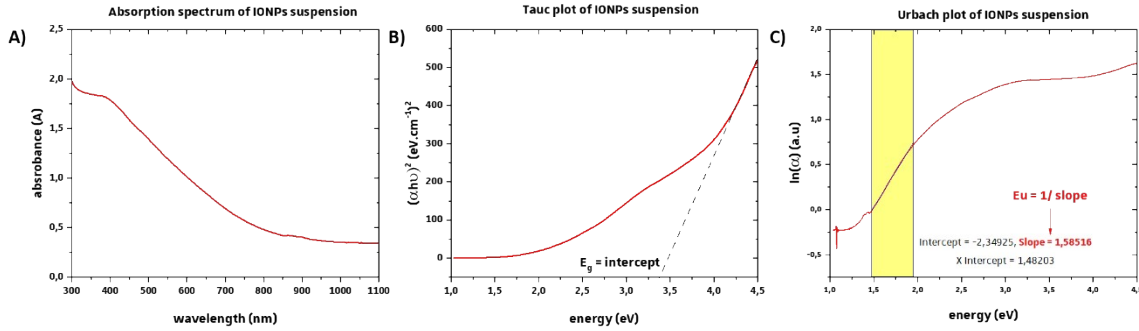


Figure S8. Characteristic examples of: A) absorption spectrum and B) Tauc plot and C) Urbach plot obtained for a 20 nm IONPs suspension at 0.05 mg Fe/mL in chloroform.

In the presence of structural defects, the band gap is not "ideal" and presents what is called an Urbach tail (Figure S8) described by the following equation:

$$\alpha = \alpha_0 \times e^{\frac{h\nu - E_g}{E_u}} \quad \#(3)$$

Where α is the absorption coefficient, α_0 is the absorption coefficient of a perfect crystal, h is the Planck constant equal to 6.63×10^{-34} J.s⁻¹, ν is the photon frequency expressed in s⁻¹, E_g is the band gap energy in J or eV and E_u is the Urbach energy in J or eV that must be determined. This equation can be rewritten as follows:

$$\ln \ln \alpha = \frac{1}{E_u} h\nu - \frac{E_g}{E_u} + \ln \ln \alpha_0 \quad \#(4)$$

Thus, $\ln \ln \alpha$ can be plotted in function of the energy $h\nu$ and the slope of the curve is equal to the inverse of E_u (Figure S9).

So comparing band gap and Urbach energy values of different batches of 20 nm IONPs should give us information about defects quantities.

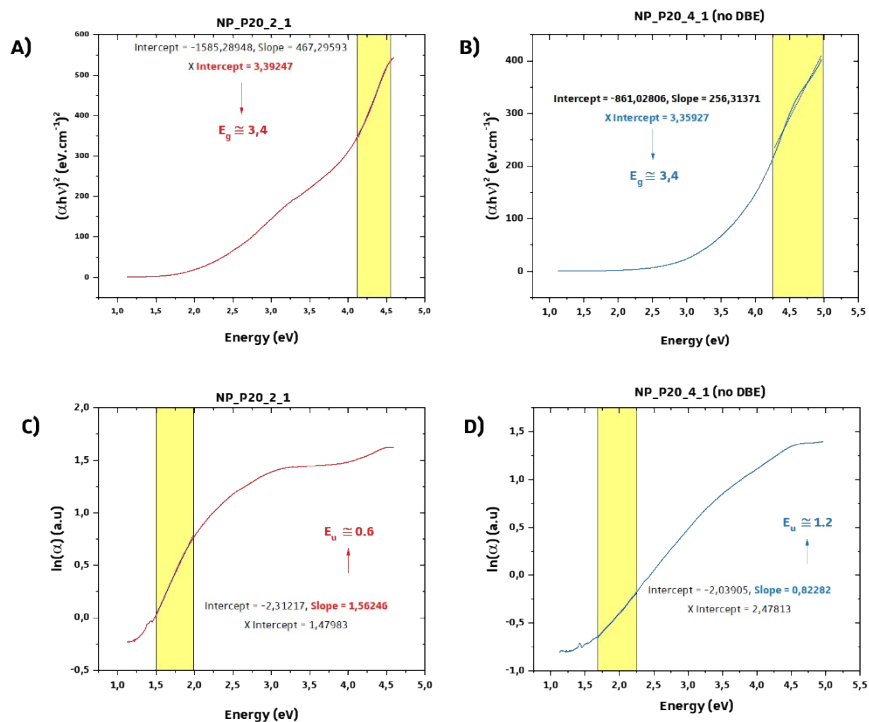


Figure S9: A) and B) Tauc plot of two IONPs batches coming from either P20_2 or P20_4_no_DBE protocols, C) and D) associated Urbach plot of the two batches.

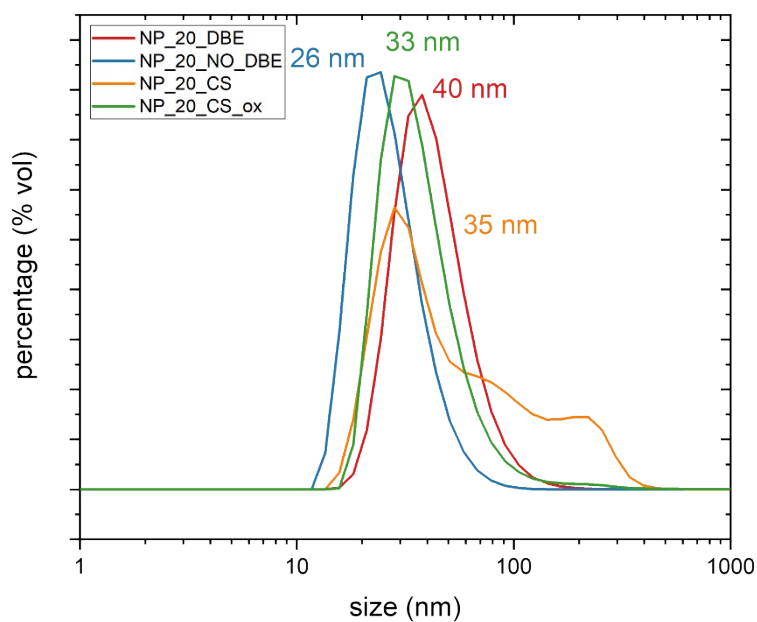


Figure S10. Volume-based nanoparticle size distribution measured by DLS for 4 samples NP_P20_DBE, NP_P20_NO_DBE, NP_P20_CS, NP_P20_CS_ox.

References

- 1 F. Perton, G. Cotin, C. Kiefer, J.-M. Strub, S. Cianferani, J.-M. Greneche, N. Parizel, B. Heinrich, B. Pichon, D. Mertz and S. Begin-Colin, *Inorg. Chem.*, 2021, **60**, 12445–12456.
- 2 G. Cotin, C. Kiefer, F. Perton, M. Boero, B. Özdamar, A. Bouzid, G. Ori, C. Massobrio, D. Begin, B. Pichon, D. Mertz and S. Begin-Colin, *ACS Applied Nano Materials*, 2018, **1**, 4306–4316.
- 3 G. Cotin, F. Perton, C. Petit, S. Sall, C. Kiefer, V. Begin, B. Pichon, C. Lefevre, D. Mertz, J.-M. Greneche and S. Begin-Colin, *Chem. Mater.*, 2020, **32**, 9245–9259.
- 4 L. M. Bronstein, J. E. Atkinson, A. G. Malyutin, F. Kidwai, B. D. Stein, D. G. Morgan, J. M. Perry and J. A. Karty, *Langmuir*, 2011, **27**, 3044–3050.
- 5 S. G. Kwon, Y. Piao, J. Park, S. Angappane, Y. Jo, N.-M. Hwang, J.-G. Park and T. Hyeon, *Journal of the American Chemical Society*, 2007, **129**, 12571–12584.
- 6 G. Cotin, B. Heinrich, F. Perton, C. Kiefer, G. Francius, D. Mertz, B. Freis, B. Pichon, J. Strub, S. Cianféran, N. Ortiz Peña, D. Ihiawakrim, D. Portehault, O. Ersen, A. Khammari, M. Picher, F. Banhart, C. Sanchez and S. Begin-Colin, *Small*, 2022, 2200414.
- 7 L. M. Bronstein, X. Huang, J. Retrum, A. Schmucker, M. Pink, B. D. Stein and B. Dragnea, *Chemistry of Materials*, 2007, **19**, 3624–3632.